

# Diagnosis of indirectly driven double shell targets with point-projection hard x-ray radiography

Cite as: Matter Radiat. Extremes 9, 027602 (2024); doi: 10.1063/5.0045112

Submitted: 23 January 2021 • Accepted: 13 November 2023 •

Published Online: 17 January 2024









View Online



Export Citation



CrossMark

Chao Tian,<sup>1</sup> Minghai Yu,<sup>1</sup> Lianqiang Shan,<sup>1</sup> Fengjuan Wu,<sup>2</sup> Bi Bi,<sup>1</sup> Qiangqiang Zhang,<sup>1</sup> Yuchi Wu,<sup>1</sup>  Tiankui Zhang,<sup>1</sup> Feng Zhang,<sup>1</sup> Dongxiao Liu,<sup>1</sup>  Weiwu Wang,<sup>1</sup>  Zongqiang Yuan,<sup>1</sup> Siqian Yang,<sup>1</sup>  Lei Yang,<sup>1</sup> Zhigang Deng,<sup>1</sup> Jian Teng,<sup>1</sup>  Weimin Zhou,<sup>1,3,a)</sup> Zongqing Zhao,<sup>1</sup> Yuqiu Gu<sup>1,3,a)</sup>  and Baohan Zhang<sup>1</sup>

## AFFILIATIONS

<sup>1</sup>Science and Technology on Plasma Physics Laboratory, Laser Fusion Research Center, China Academy of Engineering Physics, Mianyang 621900, People's Republic of China

<sup>2</sup>Joint Laboratory for Extreme Conditions Matter Properties, Southwest University of Science and Technology, Mianyang 621010, People's Republic of China

<sup>3</sup>IFSA Collaborative Innovation Center, Shanghai Jiao Tong University, Shanghai 200240, People's Republic of China

<sup>a)</sup>Authors to whom correspondence should be addressed: [zhouwm@caep.cn](mailto:zhouwm@caep.cn) and [yqgu@caep.cn](mailto:yqgu@caep.cn)

## ABSTRACT

We present an application of short-pulse laser-generated hard x rays for the diagnosis of indirectly driven double shell targets. Cone-inserted double shell targets were imploded through an indirect drive approach on the upgraded SG-II laser facility. Then, based on the point-projection hard x-ray radiography technique, time-resolved radiography of the double shell targets, including that of their near-peak compression, were obtained. The backlighter source was created by the interactions of a high-intensity short pulsed laser with a metal microwire target. Images of the target near peak compression were obtained with an Au microwire. In addition, radiation hydrodynamic simulations were performed, and the target evolution obtained agrees well with the experimental results. Using the radiographic images, areal densities of the targets were evaluated.

© 2024 Author(s). All article content, except where otherwise noted, is licensed under a Creative Commons Attribution (CC BY) license (<http://creativecommons.org/licenses/by/4.0/>). <https://doi.org/10.1063/5.0045112>

## I. INTRODUCTION

Inertial confinement fusion (ICF), a clean, safe, and economic energy source, has been the focus of a tremendous amount of research effort over the last few decades,<sup>1–7</sup> and remarkable progress in this field has been reported in the recent literature.<sup>8–12</sup> The US National Ignition Facility (NIF) has achieved a record-breaking output of 3.15 MJ of fusion energy using laser indirect drive, resulting in a “net energy gain” and achieving “fusion ignition.”<sup>12</sup> However, the current energy gain is still relatively low, and there is still a long way to go before the construction of a nuclear fusion power plant and the realization of commercial power generation.

Up until now, several ignition schemes have been developed, such as central hotspot ignition, fast ignition,<sup>13–15</sup> and shock ignition.<sup>16,17</sup> In most of these, single shell targets are used. By contrast, double shell (DS) targets,<sup>18–29</sup> with two concentric shells, an outer low-Z ablator shell, and an inner higher-Z shell containing

the noncryogenic fuel, have also been proposed for exploring ignition. There are several well-known benefits of DS targets, such as the use of noncryogenic deuterium–tritium (DT) fuel, more robust shock timing, a lower ignition temperature threshold, and a relatively low convergence.<sup>22,27</sup> Despite these advantages of DS targets, however, it is found that owing to the existence of several interfaces, hydrodynamic instabilities pose a serious problem.<sup>21</sup> Experimental studies of the hydrodynamics of DS targets have shown that the obtained yields are far below the prediction from one-dimensional clean calculations.<sup>18,19,22,26</sup>

Imaging is an important method to observe the implosion process. Backlighters produced by irradiating Sc or Fe foils with nanosecond lasers have been used to perform x-ray (<10 keV) radiography to diagnose DS target implosions.<sup>23,24,28</sup> In the past few years, higher-Z materials have also been used to generate backlighters. The generation of high-Z, 10–20 keV backlighters with the NIF 2DConA platform was demonstrated by Barrios *et al.*<sup>30</sup> This has since the

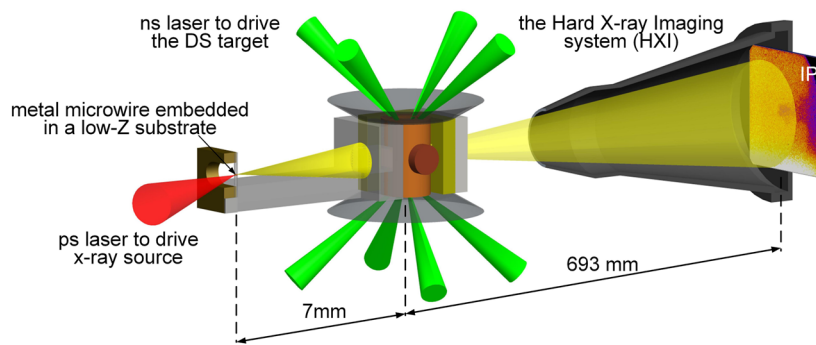


**FIG. 1.** Experimental setup for radiography experiment. The nanosecond laser pulses are injected into the hohlraum to ablate the target, and the picosecond laser pulse provides the hard x-ray backlighter. The radiographic image is captured by imaging plates (IPs) placed in the hard x-ray imaging system (HXI).

been used to obtain radiographic data of an imaging double shell target with a mid-Z inner shell on the NIF.<sup>29</sup> However, to capture the radiographic image of an ignition DS target, we need to use higher-energy x rays. Moreover, to determine the implosion processes and spatial details of the innermost shell of a three-shell target,<sup>31</sup> harder x-ray backlighters are required.

Recently, x-ray sources for radiography of dense targets based on high-intensity short-pulsed laser–solid target interactions have been demonstrated.<sup>32–40</sup> Intense x-ray bursts, including continuous bremsstrahlung emission and characteristic lines, are produced by the interactions of hot electrons with the target material after irradiation by intense lasers with intensity  $I_L > 10^{17}$  W/cm<sup>2</sup>. Since the most high-energy x rays are created in the dense, high-Z parts of the target, radiography with high spatial resolution can be comparatively easily realized by irradiating small targets or long targets with small cross sections (e.g., a metal microwire) with relativistic lasers in a point-projection geometry. This technique has already been applied in experiments on the implosions of direct drive DS targets.<sup>40</sup> However, in those experiments, the implosion performance was disappointing, and hardly any significant compression of the inner shell was observed. In this paper, we present results from an indirect drive double shell target implosion experiment using point-projection hard x-ray radiography to study the indirect drive implosion process of DS targets, which is quite different from the direct drive case. An image of the target near peak compression was obtained successfully with an Au microwire.

The remainder of the paper is organized as follows. The experimental design and setup are described in Sec. II. The main results of the experiment are presented in Sec. III and then discussed in Sec. IV. Finally, conclusions are presented in Sec. V.

## II. EXPERIMENTAL DESIGN AND SETUP

### A. Experimental setup

The experiment was carried out on the upgraded SG-II laser facility. The experimental setup is shown schematically in Fig. 1. Eight top-hat 2 ns laser beams with a total energy of about 11 kJ were injected into the hohlraum to generate x rays to implode the double shell target. A short-pulse PW laser beam irradiated the metal

microwire with 500 J energy in 10 ps to produce hard x rays. Fuji BAS-SR imaging plates (IPs) were used to record the radiographic images. To reduce background noise, the IPs were installed in a hard x-ray imaging system (HXI). The backlighter and IPs were located at 7 and 693 mm on either side of the double shell target, respectively, providing a magnification of 100× for the radiography.

Two photographs of the double shell target used in the experiment and a schematic of the target cross section are shown in Fig. 2. The double shell target was placed in the center of the hohlraum and supported by a metal cone. The hohlraum had a 25 μm-thick gold wall and 0.85 mm-diameter entrance holes of length 2.5 mm and diameter 1.6 mm. There were two 600 × 600 μm<sup>2</sup> diagnostic windows in the middle of the hohlraum for hard x rays to pass through. The double shell target had a polystyrene (CH) outer shell (80 μm thick), an Au (2 μm thick)-coated CH inner shell (15 μm thick), and an inserted Cu cone to support the inner shell. The x-ray backlighter target was a 100 μm-long metal microwire, of diameter 10 μm, embedded in a low-Z substrate.<sup>41</sup> The microwire was aligned toward the DS target, in a point-projection geometry. The backlighter was delayed by different amounts to observe the implosion process. Low-Z filters were installed between the backlighters and the hohlraum to stop electrons below ~0.4 MeV. In addition, 500 μm Cu and 500 μm Ta were placed at the back of the hohlraum to remove photons below ~100 keV. There were windows in the Cu and Ta filters to allow the x rays from the backlighter to pass through.

Figure 3 shows the layout of the experimental diagnostic equipment. In addition to the HXI, an absolutely calibrated flat-response x-ray detector (FXRD)<sup>42</sup> was used to measure the radiation flux from the laser entrance hole at one end of the hohlraum. The time sequence of the picosecond and driving lasers was measured using an x-ray streak camera (XSC).<sup>43</sup> In addition, a filter stack spectrometer (FSS)<sup>44</sup> consisting of 13 metal filters and image plates was used to measure the x-ray spectrum.

### B. Radiography simulation

Before carrying out the experiment, we construct synthetic radiographs of the implosion process of the double shell target to mimic the diagnostic capabilities. In the simulation, the backlighter

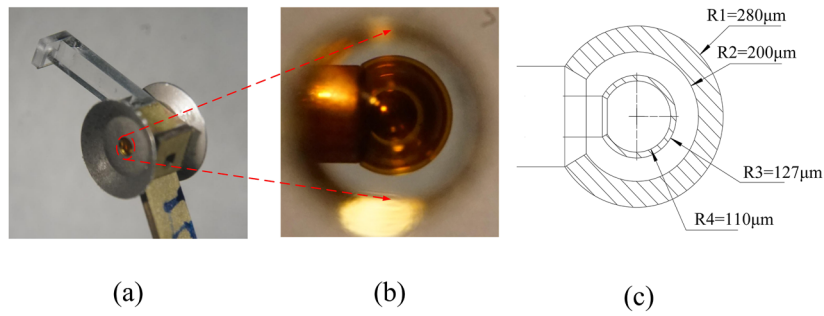


FIG. 2. (a) and (b) Photographs of indirect drive double shell target. (c) Schematic of target cross section.

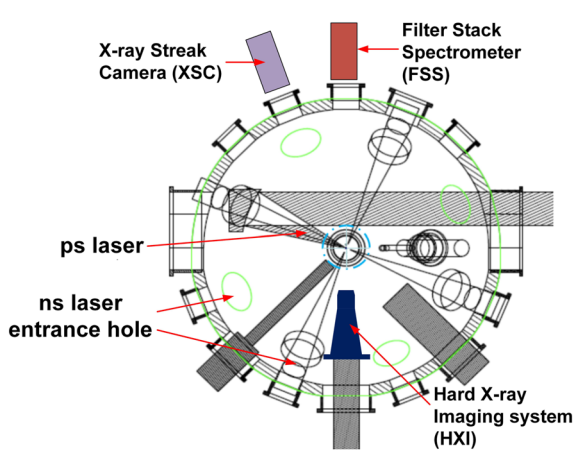


FIG. 3. Layout of experimental diagnostic equipment.

was set to a finite-size source with a size of  $10\ \mu\text{m}$  and the backlighter brightness was set to  $10^{12}$  photons/sr, according to previous experimental results. In addition, to obtain the impact of different x-ray energies on radiographic images, we used backlighters with two different types of energy spectra, one of which was monochromatic and had three different energies (8, 17.5, and 50 keV) and the other of which had the broad spectrum of the Mo microwire measured in the experiment.

First, the implosion process of the double shell target was assessed using the one-dimensional radiation hydrodynamic code Multi1D.<sup>45,46</sup> The parameters of the double shell target were the same as shown in Fig. 2(c). From the simulation results, we could obtain the density distribution at different times, from which the three-dimensional density distribution could be constructed as follows. First, a series of concentric spherical shells were generated, with the density of each shell being given by the simulated value at a location equal to the radius of the shell in the 1D simulation. Then, at the location of the support cone, part of the spherical shell was removed, and the support cone was inserted.

Then, with the three-dimensional density distribution, the Monte Carlo code GEANT4<sup>47–49</sup> was used to simulate the radiography of the double shell target at different times with x rays of

different energies. Four typical moments were selected: time A, at which the target had not yet been compressed; time B, at which the outer shell had just collided with the inner shell; time C, at which the inner shell had been compressed to half the initial size; time D, at which maximum compression was achieved. Figure 4 shows the snapshots of synthetic radiographs taken at these four typical moments, using backlighters with monochromatic 8, 17.5, and 50 keV spectra and the broad spectrum of the Mo microwire, respectively. We can see that when 8 keV x rays are used for radiography, both the outer and inner shells are revealed, but in the later stage of compression, the x rays cannot penetrate the inner shell and so no internal information about that shell can be obtained. With 17.5 keV x rays, only the inner shell is clearly shown, but at the moment of maximum compression, the inner shell layer still cannot be penetrated by the x rays. With 50 keV x rays, the contrast of the radiographic image is poor in the early stage of compression, but at the moment of maximum compression, the image contrast is good and internal information about the inner shell can be seen. When x rays with the broad spectrum of the Mo microwire are used, the simulation results are close to those obtained using 17.5 keV monoenergetic x rays, but the x rays produced by the Mo wire are slightly more penetrating. From these results, we can see that the use of the Mo backlighter is appropriate in the early and middle stages of compression.

In the following, we use the signal-to-noise ratio (SNR) to evaluate the quality of the synthetic radiographic images.<sup>50</sup> The SNR is defined as  $\text{SNR} = \Delta I / \sigma_I$ , where  $\Delta I$  is the change in intensity caused by the target and  $\sigma_I$  is the standard deviation of the background intensity.  $\sigma_I$  was determined as follows. First, we selected a region where x rays passed directly through, i.e., a region without a target. Then, the intensity of each pixel in the region was counted, and the standard deviation of the intensity in the region was calculated from the expression

$$\sigma_I = \sqrt{\frac{1}{N-1} \sum_{i=1}^N |A_i - \bar{I}|^2},$$

where  $N$  is the number of pixels,  $A_i$  is the intensity of the  $i$ th pixel, and  $\bar{I}$  is the average intensity in the region. Note that the size of the region chosen may affect the magnitude of  $\sigma_I$ . In general, the larger the selected region, the more pixels it contains, and the smaller the standard deviation of the intensity is likely to be

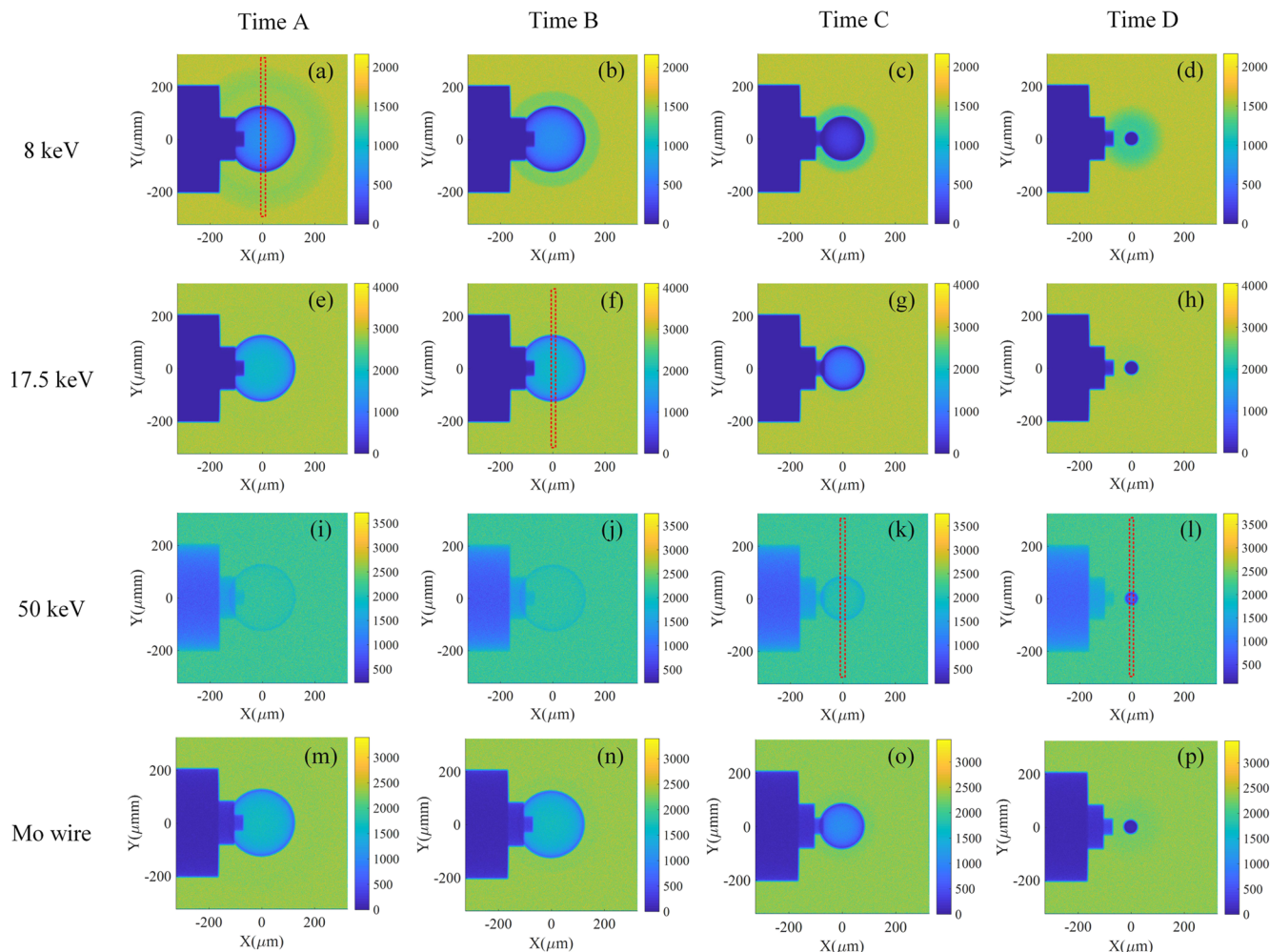


**FIG. 4.** Synthetic radiographs of the double shell target at different times with x rays of different energies. Time A: the target has not yet been compressed. Time B: the outer shell has just collided with the inner shell. Time C: the inner shell has been compressed to half the initial size. Time D: compression is maximum.

eventually converging to a stable value. We first selected a smaller area, namely, a region of size comparable to the spatial resolution, and calculated the intensity deviation in that region. Then, we chose a larger region to calculate the value, and little change was found.

Four typical images, namely, those in Figs. 4(a), 4(f), 4(k), and 4(l), were selected for analysis. A lineout through the target center was taken [marked by the red lines in Figs. 4(a), 4(f), 4(k), and 4(l)] to obtain the profile of the transmitted x-ray signal, as shown in Fig. 5. For Fig. 5(a) [corresponding to Fig. 4(a)], both the outer and inner shells are shown, and calculations show that the SNR of the outer shell is about 1, while the SNRs of the edge and center of the inner shell are 13 and 8, respectively. For Fig. 5(b) [corresponding to Fig. 4(f)], the SNR of the outer shell is less than 1, and the SNRs of the edge and center of the inner shell are 10 and 5, respectively. This indicates to us that to distinguish a certain area in the image, the SNR of that area needs to be greater than 1, and

the higher the SNR, the clearer will be the area. From Fig. 5(c) [corresponding to Fig. 4(k)], it can be seen that the variation of x-ray intensity induced in the target is smaller owing to the higher photon energy, and, more quantitatively, the SNRs at the edge and center of the inner shell are 1.8 and 0.6, respectively. This suggests that the brightness of the backlighter needs to be increased to improve the SNRs. From Fig. 5(d) [corresponding to Fig. 4(l)], it can be calculated that the SNRs at the edge and center of the target are 6.2 and 4.6, respectively, which suggests that radiography with 50 keV x rays is appropriate for the target in the late stage of compression.

On the basis of the above simulation results, we find that a backlighter with a size of  $10\ \mu\text{m}$  can distinguish the inner and outer shell structures of a double shell target, and the x-ray energy of the backlighter can significantly affect the SNR of the radiographic images. Therefore, we should carefully select the x-ray energy according to the time at which measurements are to be made. To obtain the tar-

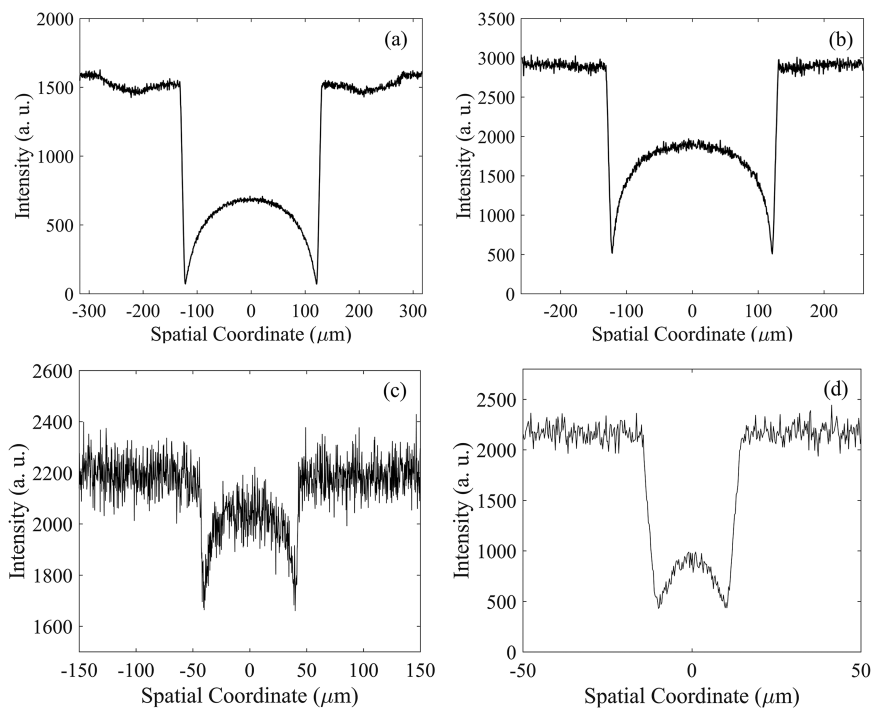


FIG. 5. (a)–(d) Synthetic transmitted x-ray signals through the target center from Figs. 4(a), 4(f), 4(k), and 4(l), respectively.

get images in the early part of the implosion, the use of Cu or Mo microwires is advantageous, whereas in the later stage, the use of Au microwires that can generate harder x rays is more appropriate. It should also be pointed out that in the present simulations, the x rays from the hohlraum were not considered, although these constitute noise in radiography and may reduce the SNR of the image. Further experiments are required to investigate this.

### III. EXPERIMENTAL RESULTS

#### A. Backlighter measurement

In the experiment, the characteristic parameters of the x-ray backlighter, such as energy spectrum and brightness, were measured. Figure 6 shows the measured x-ray spectra of different shots. In shot 105, only the short-pulse laser was used, whereas in shots 104 and 108, both the picosecond and nanosecond beams were fired. As can be seen in Fig. 6, shot 105 has the lowest x-ray intensity in the energy spectrum range below about 50 keV. This is due to the fact that in shots 104 and 108, the nanosecond laser produces a large number of lower-energy x rays. In the energy spectrum range higher than 50 keV, shot 105 has the highest x-ray intensity. Notice that the high-energy x rays come mainly from the picosecond laser interacting with the backlighter, which indicates that the nanosecond lasers can affect the backlighter and reduce the generation of high-energy x rays. Although x rays higher than 50 keV are less suitable for backlighting in the current experiment, higher-energy x rays will be needed in the future when a laser facility with higher drive energy is used with higher areal densities. This suggests that we need

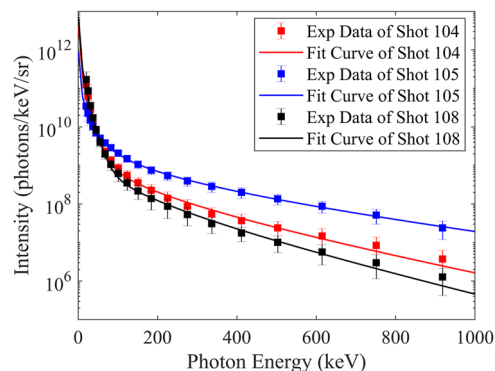


FIG. 6. Measured x-ray spectra of different shots.

to improve the target design in future experiments to reduce this impact.

Using the energy spectra, we can obtain the x-ray brightness and the energy conversion efficiency from laser to x rays. Shot 105 is analyzed here, since it was not disturbed by the nanosecond laser. In shot 105, 120  $\mu\text{m}$  Ti was placed before the image plate as a filter. Calculations show that the photon energy of x rays with transmittance higher than 5% is about 13 keV. In addition, Monte Carlo simulations show that the absorption fraction of x rays with energy higher than 100 keV in image plates is less than 7%. Therefore, we calculated the brightness and conversion efficiency of x rays in the

energy range from 13 to 100 keV, and the results are  $8.2 \times 10^{11}$  photons/sr and  $7.4 \times 10^{-5}$ , respectively. It can be seen that the brightness of the backlighter is close to that used in the simulations, which gives us confidence in obtaining radiographic images. We also find that the conversion efficiency is a bit low. This is because the use of a metal microwire target as the backlighter is inherently less efficient, owing to the fact that the majority of the laser beam passes by the wire. In addition, in the experiment, we found that there were many factors that affected the conversion efficiency, such as the targeting accuracy of the picosecond laser and the state of the focusing spot. To improve the conversion efficiency, in addition to improving the target aiming accuracy of the picosecond laser and improving the focusing state of the focal spot, V-shaped plastic structures used on NIF can also be applied to enhance the laser-wire coupling by refraction at the plasma mirror surface generated by the prepulse of the picosecond laser beam.<sup>39</sup>

In this experiment, owing to the limited number shots, the spatial resolution of the backlighter was not measured. According to previous experiments,<sup>40</sup> the spatial resolution of this backlighter is close to the wire diameter. Therefore, we believe that when using 10 and 20  $\mu\text{m}$  metal wires, the spatial resolution of the obtained images is about 10 and 20  $\mu\text{m}$ , respectively. From the simulation results, this spatial resolution enables the evolution of the inner layer to be seen. However, this spatial resolution is not sufficient if more detailed structures need to be observed, such as those occurring during the evolution of hydrodynamic instabilities. Improvement of spatial resolution is an ongoing study.

## B. Radiation temperature measurement

In the experiment, eight laser beams with 2 ns square pulse carrying a total energy of about 11 kJ were injected into the hohlraum. The laser intensity directly heated the wall of the hohlraum, and this gold wall converted the laser energy into soft x rays. These soft x rays were absorbed and re-emitted under the constraint of the hohlraum, thus forming a nearly uniform radiation field within the hohlraum. The radiation flux from the hohlraum was measured by a flat-response x-ray detector (FXRD).<sup>4</sup> The radiation temperature, which is one of the key parameters in the indirect-drive scheme, can be inferred from the measured x-ray flux, and it is shown in Fig. 7. We can see that the radiation temperature rises, steeply at first and then more gradually, reaches its peak of about 180 eV at  $\sim 2$  ns, and then decreases gradually.

## C. Time delay between picosecond and nanosecond laser beam measurements

By adjusting the time delay between the picosecond laser and nanosecond laser, implosion images at different times were obtained by radiography. Therefore, to obtain a radiographic image at a specific time, the time delay is very important. In the experiment, the time delay was measured by an XSC.<sup>43</sup> The “soft x-ray” signal produced by the nanosecond laser was imaged by an image slit, while “hard x rays” created by the picosecond laser could easily penetrate the slit board and illuminate the whole cathode. In addition, the two kinds of x rays were produced at different positions. Therefore, the image areas from the two kinds of x rays in the cathode were quite different, and it was possible to measure the time delay between the picosecond and nanosecond laser beams.

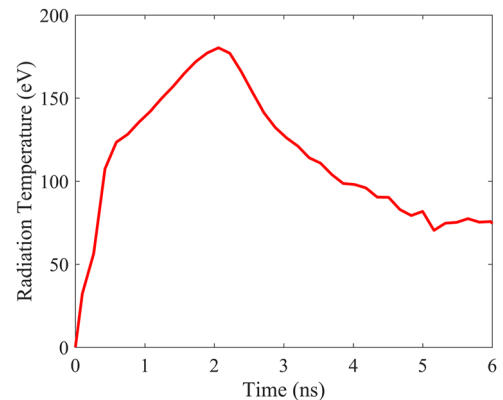


FIG. 7. Measured time history of hohlraum radiation temperature.

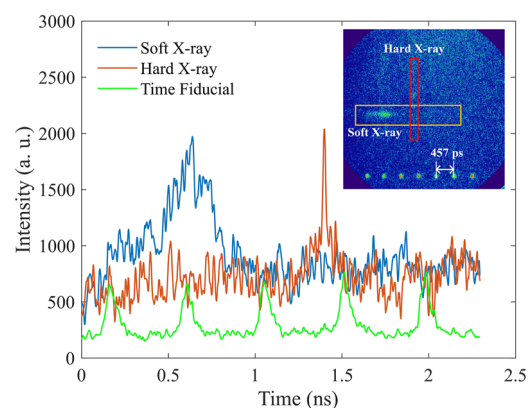


FIG. 8. X-ray signals from the picosecond and nanosecond laser beams in shot 104. The optical fiducial pulses synchronized with the nanosecond laser are also presented.

A typical experimental result in shot 104 is shown in Fig. 8. The inset in the upper right of the figure shows the original result from the XSC, and gives the “soft x-ray” and “hard x-ray” signals. The optical fiducial pulses are also presented, with a time interval of 457 ps. The “soft x-ray,” “hard x-ray,” and optical fiducial pulse histories extracted from the original image are given by the three curves. The “soft x-ray” duration corresponds to the radiation process inside the hohlraum, which is consistent with that recorded by the FXRD. It can be found from the figure that the time delay between the “soft x-ray” and “hard x-ray” peaks is about 760 ps.

It can also be seen from Fig. 8 that the “hard x-ray” pulse duration is about 28 ps, which means that the time resolution of the backlighter is also about this order of magnitude. The implosion velocity of the inner shell inferred from the simulations is about 76 km/s, and so the blur caused by the motion is about 2.2  $\mu\text{m}$ . Noting that the spatial resolution of the backlighter is about 10  $\mu\text{m}$ , it can be considered that motion blur has little effect on the radiographic images.

## D. Radiography results

First, to get a radiograph of an un-driven target, only the short pulse laser was fired. A 10  $\mu\text{m}$  Mo microwire was used as the backlighter. The radiography result is presented in Fig. 9(a), showing both the inner shell and the supporting cone clearly. From the figure, the radius of the inner shell is found to be about 126  $\mu\text{m}$ , which is very close to the design parameters of the target. Then, picosecond and nanosecond beams were all fired, and the delay of the picosecond pulse was adjusted. With a 10  $\mu\text{m}$ -diameter Mo microwire backlighter, we acquired a radiograph at time  $t = 2.76$  ns, as given in Fig. 9(b), which shows that the inner shell was slightly compressed. To obtain a profile of a highly compressed target, we used a thicker and higher- $Z$  microwire, namely, a 20  $\mu\text{m}$ -diameter Au microwire backlighter. The picosecond pulse was fired at  $t = 4.45$  ns according to radiation-hydrodynamic simulations, and one image of the target near peak compression was obtained successfully, as shown in Fig. 9(c).

To evaluate the quality of the radiographic images, several line-outs were taken [marked by the white and black lines in Figs. 9(a) and 9(c)] to obtain the profiles of the transmitted x-ray signal and to calculate the SNRs. For Fig. 9(a), the SNR of the supporting copper cylinder (marked by the white dashed line) is about 12, and the SNR of the inner shell (marked by the black solid line) is about 5.4. For Fig. 5(c), the SNR of the inner shell (marked by the black solid line) is about 2.7.

Beside the radiographic images, colorbars with the photostimulated luminescence values (PSLs) are shown. In Fig. 9(c), the PSLs are lower than those in the others, since the filters placed before the image plates were different. For Mo microwire backlighters [Figs. 9(a) and 9(b)], a 120  $\mu\text{m}$  Ti filter was used, whereas for the Au microwire backlighter [Fig. 9(c)], 60  $\mu\text{m}$  Ti and 50  $\mu\text{m}$  Cu filters were used. These filters can block low-energy x rays that arise mostly from the hohlraum, thus increasing the signal-to-background ratio.

## IV. DISCUSSION

### A. Coupling efficiency and radiation asymmetry

For indirectly driven double shell targets, energy transfer includes the following processes: first, laser energy is converted into x-ray energy in the hohlraum; then, x-rays are absorbed by the outer shell; next, the outer shell collides with the inner shell to transfer energy to the inner shell; finally, the inner shell compresses the fuel and converts its kinetic energy into internal energy of the fuel. The first process has already been thoroughly investigated.<sup>2-4</sup> Generally speaking, for an Au hohlraum, the energy conversion efficiency  $\eta_{ce}$  from laser to x-ray can reach over 75%.<sup>3,4</sup> The coupling efficiency from the hohlraum to the capsule depends mainly on a geometric parameter, namely, the ratio of the surface area of the capsule to that of the hohlraum.<sup>51,52</sup> In our target design, the length and diameter of the hohlraum were 2.5 and 1.6 mm, respectively, while the outer diameter of the double shell target was 560  $\mu\text{m}$ , which is similar to that used by Robey *et al.*<sup>26</sup> on the OMEGA laser facility. This target design leads to a case-to-capsule ratio (CCR, defined as the ratio of the hohlraum diameter to the outer diameter of the capsule) of 2.86. The difference is that in our experiment, there were two  $600 \times 600 \mu\text{m}^2$  diagnostic windows in the middle of the hohlraum

for hard x rays to pass through. This will reduce the coupling efficiency of the hohlraum to the capsule. The coupling efficiency from hohlraum to capsule is defined as<sup>51</sup>

$$\eta_{HC} = \frac{(1 - \alpha_C)A_C}{(1 - \alpha_W)A_W + (1 - \alpha_C)A_C + A_L + A_D},$$

where  $\alpha_W$  is the wall albedo,  $\alpha_C$  is the capsule albedo,  $A_W$  is the hohlraum wall area,  $A_C$  is the capsule area,  $A_L$  is the laser entrance hole (LEH) area, and  $A_D$  is the diagnostic window area. To estimate  $\eta_{HC}$ , we take  $\alpha_W = 0.8$  and  $\alpha_C = 0.3$ , and calculations then show that the value of  $\eta_{HC}$  for the current hohlraum is 12.9%. If there were no diagnostic windows,  $\eta_{HC}$  would increase to 14%.

Figure 9(b) shows that the compression of the target is asymmetric, with more compression at the poles than at the equator. We suspect that this was caused by asymmetric driving of hohlraum radiation, and therefore the radiation flux distributions on the capsule surface were examined.

The radiation asymmetry was evaluated by IRAD3D,<sup>53</sup> which is a 3D view-factor code and can provide the radiation flux on the capsule under a variety of conditions. Using the size of the hohlraum and the injection angle and energy of each laser beam, the radiation flux distribution on the surface of the capsule as calculated by IRAD3D is shown in Fig. 10. It can be seen that the radiation flux at the poles of the target is stronger than that at the equator, which is consistent with the radiographic result that the poles of the target were compressed more. In addition, the radiation flux at the equatorial position near the diagnostic windows is weak. This shows that the diagnostic windows have an influence on the radiation field distribution in the hohlraum. Besides, as discussed earlier, the diagnostic windows reduced the coupling efficiency of the hohlraum to the capsule. In the future, we will consider using a hohlraum without diagnostic windows to improve the coupling efficiency and realize a more uniform radiation field. Owing to the high energy of the x rays from the backlighter, it is possible for them to pass through the hohlraum wall and obtain radiographic images of the double shell target.

### B. Implosion and shell evolution

On the basis of the measured radiation temperature, numerical simulations were carried out, and the implosion and shell evolution were analyzed. The radiation hydrodynamic simulation was performed using Multi1D, and the implosion trajectory is shown in Fig. 11(a) by the thin curves. The green, red, and blue lines represent the inner shell, outer shell, and Au coating layer, respectively. The density distribution and its evolution with time are presented in Fig. 11(b).

The simulation results show that the imploding outer shell collides with the inner one at about  $t = 2.7$  ns, and the inner shell stagnates at about  $t = 4.36$  ns. Therefore, we chose these two moments for diagnosis. In shot 104, the picosecond laser was fired at  $t = 2.76$  ns. From the radiographic image shown in Fig. 9(b), we see that the inner shell was compressed into an elliptical shape with radii of about 119  $\mu\text{m}$  in the horizontal direction and 101  $\mu\text{m}$  in the vertical direction. This shows that in the experiment, the target poles were compressed faster than in the simulation. This may be due to the uneven distribution of the radiation field on the target surface, with a greater radiation flux irradiating the

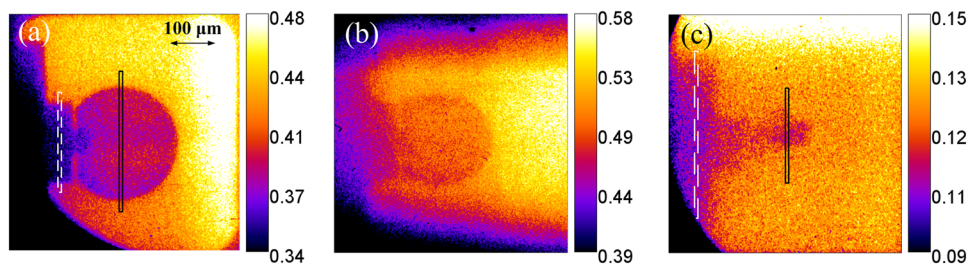


**FIG. 9.** Time-resolved radiographic images of indirectly driven double shell targets. (a) Shot 105, only short-pulse laser, un-driven target. (b) Shot 104,  $t = 2.76$  ns. (c) Shot 108,  $t = 4.45$  ns.

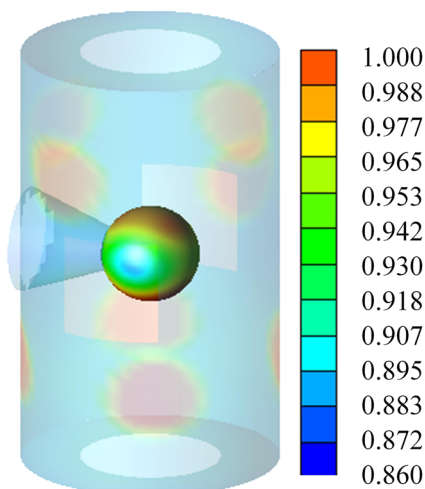


**FIG. 10.** Calculated normalized radiation flux distribution on the capsule.

poles of the target. In shot 108, the picosecond laser was fired at  $t = 4.45$  ns. From the radiographic image at this moment [Fig. 9(c)], it is found that the radius of the compressed target is about  $25 \mu\text{m}$ , which is slightly larger than the simulated radius of about  $20 \mu\text{m}$ . This is understandable, because the actual implosion is not an ideal one-dimensional implosion.

On the basis of the radiation flux distribution on the capsule surface obtained in Sec. IV A, the contour evolution of the inner shell was analyzed. First, using the distribution shown in Fig. 10, the radiation flux distribution on the cross section of the target viewed from the HXI was calculated. A series of 1D radiation-hydrodynamics simulations with Multi1D were then carried out using the radiation flux at different positions on the cross section, and the radii at different polar angles were obtained. In this way, the cross-sectional shape of the inner shell was determined, as shown in Fig. 12. For comparison, the data contour of the experimental results from Fig. 9(b) is also shown by the dashed line.

### C. Areal density analysis

In this subsection, we evaluate the areal density. In contrast to the case of a monochromatic source, the areal density cannot be

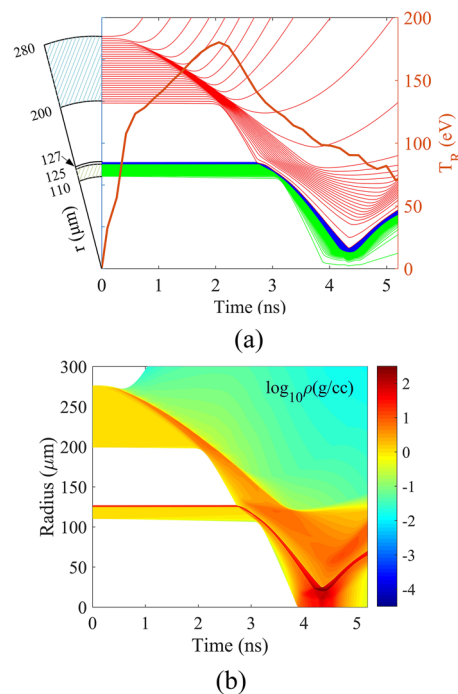


**FIG. 11.** (a) Schematic of DS target design, and simulated implosion trajectory of the indirect drive DS target. (b) Density distribution and its evolution with time.

directly obtained from transmission. The reason is that the transmissions of hard x rays vary with the spectrum; in addition, the image plate's response to incident photons is strongly impacted by their energies.<sup>36</sup> Therefore, we conducted a series of Monte Carlo simulations with GEANT4 to evaluate the phonon-to-plate response, with the result displayed in Fig. 13; then, by combining the response with the measured spectrum (shown in Fig. 6), the full response of the imaging system can be obtained. By using the full response, the relation between different areal densities and transmittance can be calculated. Therefore, once the transmittance of a certain area is known, the areal density distribution in this area can be inferred.

In shot 105 [Fig. 9(a)], only the short-pulse laser was fired. It should be pointed out that though only the PW laser was employed,



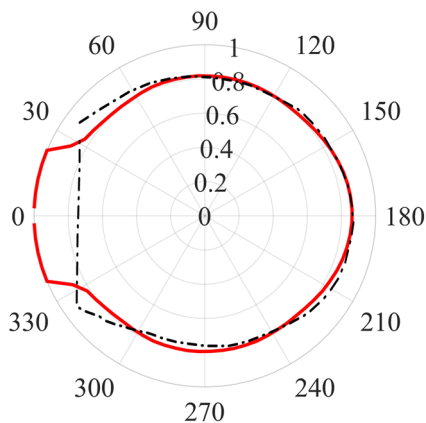


**FIG. 12.** Predicted cross-sectional shape of the inner shell. The dashed line represents the data contour from Fig. 9(b).

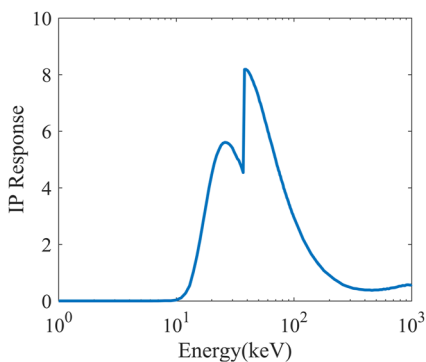


**FIG. 13.** Response of image plates to photons with different energies.

the unwanted hot electrons produced by the short pulse would hit the Au hohlraum, and generate x rays, forming background noise on the image plate. Thus, it is necessary to subtract the background when calculating the x-ray transmission through the target. The supporting copper cylinder [marked by the dashed box in Fig. 9(a)] can be used as an on-shot calibration to estimate the background level. Using the full response of the imaging system, we calculated the transmission for the copper cylinder at different spatial coordinates, as shown by the black curve in Fig. 14(a). In addition, the x-ray transmission through the copper cylinder could be obtained from the experimental results. After subtraction of an appropriate background, the measured transmission is given in Fig. 14(a) for comparison, depicted by the red curve. We can see that in the central region, the measured profile agrees well with the simulated value, indicating that the subtracted background is reasonable. It can also be seen that, unlike the experimental data, the simulated profile shows a sharp edge at the cylinder border. This is because in our calculation, a point backlighter was assumed, whereas in reality, the x-ray backlighter has finite size, and the source size can affect the transmission profile.<sup>54</sup>

With the estimated background level, the areal density of the un-driven target shown in Fig. 9(a) can be analyzed. After subtraction of the background, the transmission is obtained. We can then find the areal density distribution with the full response of the HXI, as shown in Fig. 14(b). The solid curve was obtained using the radiographic image, and further smoothing gave the dashed curve. Note that the areal density given here is mainly contributed by the gold layer. This is because the x-ray energy of the backlighter is high, and there is almost no deposition energy when it passes through the plastic shells. According to the design, the initial areal density in the central region of the target is about 7.7 mg/cm<sup>2</sup>. The inferred areal density at the same position is about 7.5 mg/cm<sup>2</sup>, quite close to the design data. Besides, the areal density is expected to increase radially. Both the numerical value and the trend are in good agreement with those shown in Fig. 14(b).

The areal density near the peak compression in Fig. 9(c) was estimated in the same way. A lineout across the center of the target was applied to obtain the transmitted x-ray signal, the raw data of which are plotted in Fig. 15(a). From Fig. 9(c), we can see that the copper cylinder near the target has been ablated, making it difficult to evaluate its areal density distribution. Therefore, a region of the larger-diameter cylinder (marked by the dashed box) was chosen and used as an on-shot calibration to estimate the background level. With the same method as above, we can obtain the areal density of the compressed target, as displayed in Fig. 5(b), indicating that the peak value of the smoothed curve is about 70 mg/cm<sup>2</sup>.

Now, we estimate the uncertainty of the areal density obtained by this method. The areal density of the target near peak compression is analyzed as an example. The uncertainty comes mainly from two sources, namely, the uncertainty in the energy spectrum measurement and that in the transmittance. The measured energy spectrum is shown in Fig. 6, in which the error bars reflect the uncertainty of measurement. To evaluate the influence of the energy spectrum uncertainty on the areal density, a series of energy spectra were generated by the Monte Carlo method, as shown in Fig. 16(a) (only 100 of them are presented as examples), in which the intensity distribution corresponding to each energy point satisfies a normal distribution, with its mean and variance being given by the measurement results. Then, for each energy spectrum, in combination with the responses of the image plates, the full response of the imaging system is obtained, and then the relationship between different areal densities and the transmittance is obtained. Through statistical analysis of this series of relationships, the average transmittance and its uncertainty distribution corresponding to different areal densities are obtained, as shown in Fig. 16(b).

Next, the uncertainty of the transmittance is analyzed. The transmittance  $T$  is calculated as  $T = (I - I_{BG}) / (I_0 - I_{BG})$ , where  $I$ ,  $I_0$ , and  $I_{BG}$  are the intensities of the target region, the region without target and the background, respectively. The relative uncertainty of the transmittance can then be calculated as  $\sigma_T = \frac{1}{T} \sqrt{\left(\frac{\partial T}{\partial I}\right)^2 (\Delta I)^2 + \left(\frac{\partial T}{\partial I_0}\right)^2 (\Delta I_0)^2 + \left(\frac{\partial T}{\partial I_{BG}}\right)^2 (\Delta I_{BG})^2} \approx 25.8\%$ , where  $\Delta I$ ,  $\Delta I_0$ , and  $\Delta I_{BG}$  are the uncertainties in  $I$ ,  $I_0$ , and  $I_{BG}$ , which can be obtained from Fig. 9(c).

For a given transmittance, the areal density can be obtained by using the relationship between transmittance and areal density

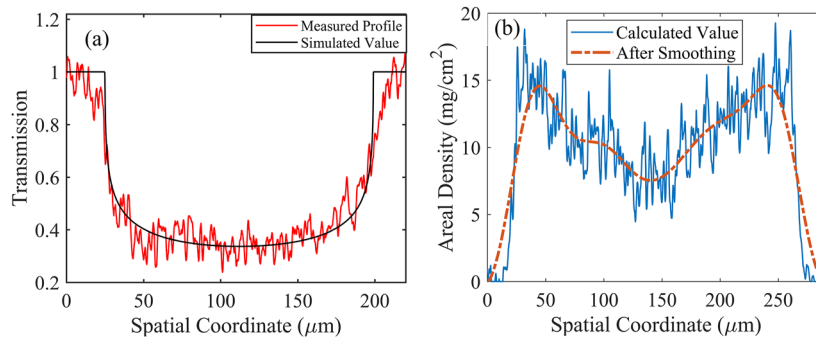


**FIG. 14.** (a) Calculation of the transmission profile through the copper cylinder (black curve), and the measured profile from the experimental results (red curve). (b) Areal density distribution of the un-driven target. The solid curve was obtained using the radiography data, and further smoothing gave the dashed curve.

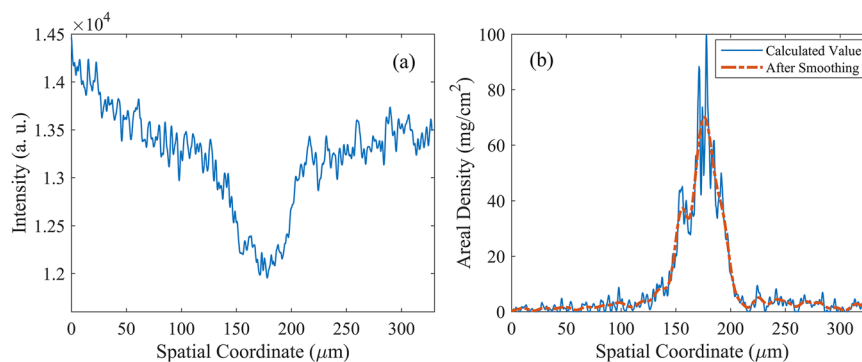


**FIG. 15.** (a) Intensity of PSL data through the target center region shown in Fig. 9(c). (b) Areal density distribution obtained near peak compression. The solid curve was calculated from the radiographic image, and further smoothing gave the dashed curve.

shown in Fig. 16(b). Owing to the existence of uncertainties in both the transmittance and the relationship, the Monte Carlo method is used to evaluate the impact of these uncertainties on the areal density. Series of transmittances and relationships, with the distribution satisfying the uncertainty requirements, are generated. For each transmittance and each relationship, the areal density can be calculated. Then, the distribution of these areal densities is analyzed, and the mean value and relative uncertainty are found to be  $72 \text{ mg/cm}^2$  and 32.6%, respectively.

It is also possible to derive the areal density based on the size of the compressed target. From Fig. 9(c), we find that the radius of the compressed inner shell is about  $25 \mu\text{m}$ , and therefore the compression ratio (CR) is about 5. As the areal density is proportional to  $\text{CR}^2$ , the compressed areal density is inferred to be  $25 \times 7.7 = 192.5 \text{ mg/cm}^2$ . It should be noted that this calculation makes two implicit assumptions: (1) the mass of the target remains constant before and after compression; (2) the compression process of the target is close to the one-dimensional ideal compression. The first assumption is valid because the current areal density is mainly contributed by the gold layer, and, according to the simulation results, at the moment close to the maximum compression, there is still CH remaining on the outside of the gold layer, and so the gold layer is not ablated and the mass before and after the

compression is unchanged. If the second assumption, namely, that the compression process is close to one-dimensional ideal compression, is assumed to be valid, then the areal density calculated by this method should be close to that of the one-dimensional simulation. The simulation results from Multi1D show that the areal density at  $t = 4.45 \text{ ns}$  is about  $195 \text{ mg/cm}^2$ , close to the value inferred from the size of the compressed target. In practice, however, the second assumption is not necessarily valid. As shown in Fig. 9(c), the shape of the compressed target is not an ideal circle. This makes it difficult to determine its size. The current method is to take the FWHM of the intensity distribution in the black box in Fig. 9(c) as its radius. Since the compression is not actually an ideal one-dimensional compression, this method gives a higher areal density than the result from the radiographic image.

From the above analysis, we find that after taking into account the measurement error in the energy spectrum and the uncertainty in the transmittance, the evaluated areal density is still lower than that given by one-dimensional simulation within the error range. There are several reasons for this. The main reason is that in reality, it is very difficult to achieve a perfectly one-dimensional implosion. Moreover, the inserted supporting cone breaks the spherical symmetry of the target. Another reason is that the subtracted background will affect the inferred areal density. In the present experiment, the

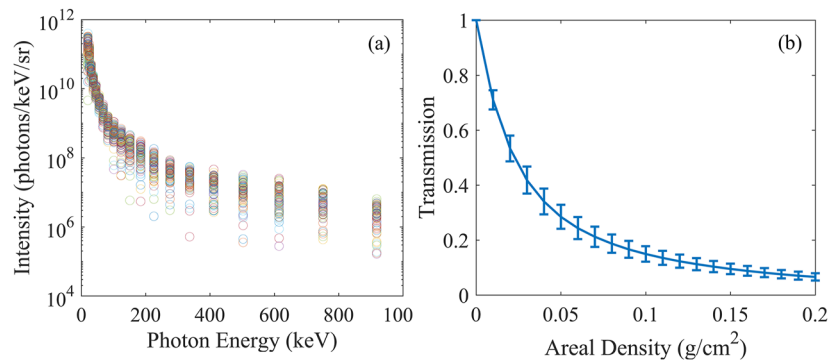


**FIG. 16.** (a) A series of energy spectra obtained by the Monte Carlo method. (b) Average transmittance and its uncertainty distribution corresponding to different areal densities.

viewing angle of the FSS for measuring the x-ray spectrum was different from that of the HXI. This means that the measured energy spectrum may differ somewhat from the x-ray spectrum for radiography, and this can result in errors in calculating the full response of the imaging system. According to the results of previous experiments, in general, closer to the direction of laser propagation, the produced x rays will be a bit brighter and have more high-energy photons. Therefore, if the energy spectrum measured in the HXI direction were to be used for evaluation, the areal density obtained would be a little higher. Besides, we assumed that the supporting copper cylinder in Fig. 9(c) was not affected by the hohlraum x rays, but it may actually be irradiated. All of these factors will have an impact the background level and hence the areal density estimation. In future experiments, we will consider using additional types of spectral diagnostic equipment to improve the measurement accuracy, measuring the energy spectra of x rays at multiple angles in order to remove the effect of angular dependence, measuring the energy spectra of x rays generated by the nanosecond and picosecond lasers separately in the direction of the radiography, and using more on-line calibration objects, such as steps with different thicknesses and materials, in order to make a more accurate assessment of the background. In addition, radiography of the implosion process from multiple angles facilitates a more accurate assessment of the symmetry of the implosion, as well as helping to evaluate the density distribution.

#### D. Comparison with direct drive

From Fig. 9, we can see that the radiographic image quality when both the picosecond and nanosecond beams were fired is worse than that when only the picosecond beam was on. There are two main reasons. One is that the nanosecond laser beams ablated the backlighter target, reducing hard x-ray production.<sup>40</sup> Another reason is that x rays generated by the nanosecond laser irradiate the hohlraum and the double shell target, generating strong noise.

Similar phenomena were also observed in previous experiments on radiography of directly driven double shell targets. However, we find that there are significant differences between the direct and indirect drive cases. First, the influence of the nanosecond laser on

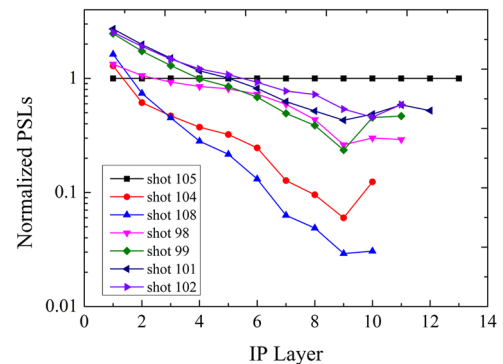


**FIG. 17.** Comparison of PSLs on the FSS IPs from different shots.

the brightness of the backlighter is different under these two different driving conditions. In the experiment, the FSS was used to measure the backlighter spectrum, and the PSLs on different IP layers of the FSS were positively correlated with the intensities of x rays with different energies. Therefore, we can use the PSL values on different layer IPs to characterize the intensity of x rays with different energies. Figure 17 shows the PSLs on the FSS IPs from different shots, where the first few IPs correspond to lower-energy x rays, and the later IPs record the signals of high energy x rays. Shots 104 and 108 were indirectly driven and shots 98–102 were directly driven, and for comparison, the results of all shots have been normalized using the results of shot 105. It is clear from the figure that the backlighter in the indirect drive case has the lowest yield of high-energy x rays. This is because in the case of indirect drive, not only does the unconverted nanosecond laser have an impact on the backlighter, but also the x rays leaking from the hohlraum diagnostic windows cause ablation of the backlighter, thus creating a pre-plasma on its surface, expanding the hot-electron dispersion angle and reducing the amount of high-energy x-ray production.

It should also be pointed out that direct drive and indirect drive produce different types of noise, and so it is necessary to analyze the noise sources and adopt corresponding shielding

methods. For direct drive, the noise comes mainly from the interaction between the laser beams and the low- $Z$  ablation layer, which produces x rays with relatively low energy, but a large number of photons. For indirect drive, the noise comes mainly from the laser entrance holes, the diagnostic windows, and the interaction between the hohlraum and the hot electrons generated by laser–plasma interaction. Therefore, for indirect drive, more shielding methods are needed. In the future, we will try to improve the design of the target to raise the hard x-ray flux, strengthen the shielding from the unconverted nanosecond laser and hohlraum-generated x rays to avoid ablation of the backlighter, and employ time gating techniques<sup>55</sup> to mitigate noise.

## V. CONCLUSIONS

Indirectly driven double shell target implosions have been radiographed using ultrashort-laser-excited hard x rays. Images of the double shell target at different moments have been obtained. The shell evolution and the compressed shell radius deduced from the radiographic images agree well with the radiation hydrodynamic simulations. Specific areal density analyses have also been investigated. The inferred areal density and its trend of change for an un-driven target are consistent with the target design. The inferred maximum areal density of the compressed target is about  $72 \text{ mg/cm}^2$ , which is lower than the simulated value. The possible causes of this discrepancy have been discussed. Furthermore, it is found that the nanosecond lasers have a negative effect on image quality, and the reasons for this degradation in image quality have been analyzed. Several methods to improve the quality of radiography have been proposed, which would help us to understand the hydrodynamics of the implosion process better.

## ACKNOWLEDGMENTS

The authors would like to thank the crew and support staff of the upgraded SG-II laser facility for operational support and the target fabrication team for their contributions to this work. The authors would also like to thank Dr. Bo Zhang, Dr. Zhaohui Wu and Dr. Longfei Jing for fruitful discussions and for polishing the manuscript. This work is supported by the National Key R&D Program of China (Grant Nos. 2022YFA1603300 and 2022YFA1603200), the Science Challenge Project (Grant No. TZ2018005) in China, the National Natural Science Foundation of China (Grant Nos. 11805188 and 12175209), and the Laser Fusion Research Center Funds for Young Talents (Grant No. RCFPD6-2022-1).

## AUTHOR DECLARATIONS

### Conflict of Interest

The authors have no conflicts to disclose.

### Author Contributions

**Chao Tian:** Conceptualization (equal); Data curation (lead); Investigation (equal); Writing – original draft (lead). **Minghai Yu:** Investigation (equal); Methodology (equal). **Lianqiang Shan:** Data

curation (equal); Investigation (equal); Methodology (equal). **Fenguan Wu:** Data curation (equal). **Bi Bi:** Data curation (equal); Investigation (equal). **Qiangqiang Zhang:** Methodology (equal). **Yuchi Wu:** Conceptualization (equal); Data curation (equal); Supervision (equal). **Tiankui Zhang:** Data curation (equal); Investigation (equal). **Feng Zhang:** Methodology (equal). **Dongxiao Liu:** Methodology (equal). **Weiwu Wang:** Data curation (equal); Investigation (equal). **Zongqiang Yuan:** Data curation (equal); Investigation (equal). **Siqian Yang:** Data curation (equal); Investigation (equal). **Lei Yang:** Methodology (equal). **Zhigang Deng:** Investigation (equal); Methodology (equal). **Jian Teng:** Investigation (equal); Methodology (equal). **Weimin Zhou:** Conceptualization (equal); Funding acquisition (lead). **Zongqing Zhao:** Conceptualization (equal); Supervision (equal). **Yuqiu Gu:** Conceptualization (equal); Supervision (equal). **Baohan Zhang:** Supervision (equal).

## DATA AVAILABILITY

The data that support the findings of this study are available upon reasonable request from the authors.

## REFERENCES

- 1 J. H. Nuckolls, L. Wood, A. Thiessen, and G. B. Zimmerman, “Laser compression of matter to super-high densities: Thermonuclear (CTR) applications,” *Nature* **239**, 139 (1972).
- 2 J. Lindl, “Development of the indirect-drive approach to inertial confinement fusion and the target physics basis for ignition and gain,” *Phys. Plasmas* **2**, 3933 (1995).
- 3 S. Atzeni and J. Meyer-ter-Vehn, *The Physics of Inertial Fusion: Beam Plasma Interaction, Hydrodynamics, Hot Dense Matter* (Oxford University Press, Oxford, 2004).
- 4 J. D. Lindl, P. Amendt, R. L. Berger *et al.*, “The physics basis for ignition using indirect-drive targets on the National Ignition Facility,” *Phys. Plasmas* **11**, 339 (2004).
- 5 J. Lindl, O. Landen, J. Edwards, and E. Moses, “Review of the national ignition campaign 2009–2012,” *Phys. Plasmas* **21**, 020501 (2014).
- 6 S. Jacquemot, “Inertial confinement fusion for energy: Overview of the ongoing experimental, theoretical and numerical studies,” *Nucl. Fusion* **57**, 102024 (2017).
- 7 R. Betti and O. A. Hurricane, “Inertial-confinement fusion with lasers,” *Nat. Phys.* **12**, 435 (2016).
- 8 O. A. Hurricane, D. A. Callahan, D. T. Casey *et al.*, “Fuel gain exceeding unity in an inertially confined fusion implosion,” *Nature* **506**, 343 (2014).
- 9 L. Q. Shan, H. B. Cai, W. S. Zhang *et al.*, “Experimental evidence of kinetic effects in indirect-drive inertial confinement fusion hohlraums,” *Phys. Rev. Lett.* **120**, 195001 (2018).
- 10 S. Le Pape, L. F. Berzak Hopkins, L. Divol *et al.*, “Fusion energy output greater than the kinetic energy of an imploding shell at the National Ignition Facility,” *Phys. Rev. Lett.* **120**, 245003 (2018).
- 11 V. Gopalaswamy, R. Betti, J. P. Knauer *et al.*, “Tripled yield in direct-drive laser fusion through statistical modelling,” *Nature* **565**, 581 (2019).
- 12 H. Abu-Shawareb, R. Acree, P. Adams *et al.*, “Lawson criterion for ignition exceeded in an inertial fusion experiment,” *Phys. Rev. Lett.* **129**, 075001 (2022).
- 13 M. Tabak, J. Hammer, M. E. Glinsky *et al.*, “Ignition and high gain with ultrapowerful lasers,” *Phys. Plasmas* **1**, 1626 (1994).
- 14 H. Azechi, K. Mima, Y. Fujimoto *et al.*, “Plasma physics and laser development for the fast-ignition realization experiment (FIREX) project,” *Nucl. Fusion* **49**, 104024 (2009).
- 15 W. Theobald, A. A. Solodov, C. Stoeckl *et al.*, “Initial cone-in-shell fast-ignition experiments on OMEGA,” *Phys. Plasmas* **18**, 056305 (2011).
- 16 R. Betti, C. D. Zhou, K. S. Anderson *et al.*, “Shock ignition of thermonuclear fuel with high areal density,” *Phys. Rev. Lett.* **98**, 155001 (2007).

- <sup>17</sup>K. S. Anderson, R. Betti, P. W. McKenty *et al.*, “A polar-drive shock-ignition design for the National Ignition Facility,” *Phys. Plasmas* **20**, 056312 (2013).
- <sup>18</sup>Y. Kitagawa, N. Miyanaga, H. Hama *et al.*, “Double-shell-target implosion by four beams from the GEKKO IV laser system,” *Phys. Rev. Lett.* **51**, 570 (1983).
- <sup>19</sup>W. S. Varnum, N. D. Delamater, S. C. Evans *et al.*, “Progress toward ignition with noncryogenic double-shell capsules,” *Phys. Rev. Lett.* **84**, 5153 (2000).
- <sup>20</sup>P. Amendt, J. D. Colvin, R. E. Tipton *et al.*, “Indirect-drive noncryogenic double-shell ignition targets for the National Ignition Facility: Design and analysis,” *Phys. Plasmas* **9**, 2221 (2002).
- <sup>21</sup>J. L. Milovich, P. Amendt, M. Marinak, and H. Robey, “Multimode short-wavelength perturbation growth studies for the National Ignition Facility double-shell ignition target designs,” *Phys. Plasmas* **11**, 1552 (2004).
- <sup>22</sup>P. Amendt, H. Robey, H. S. Park *et al.*, “Hohlraum-driven ignitionlike double-shell implosions on the omega laser facility,” *Phys. Rev. Lett.* **94**, 065004 (2005).
- <sup>23</sup>G. A. Kyrala, N. D. Delamater, D. C. Wilson *et al.*, “Direct drive double shell target implosion hydrodynamics on OMEGA,” *Laser Part. Beams* **23**, 187 (2005).
- <sup>24</sup>G. A. Kyrala, M. A. Gunderson, N. D. Delamater *et al.*, “Detailed diagnosis of a double-shell collision under realistic implosion conditions,” *Phys. Plasmas* **13**, 056306 (2006).
- <sup>25</sup>P. Amendt, C. Cerjan, A. Hamza *et al.*, “Assessing the prospects for achieving double-shell ignition on the National Ignition Facility using vacuum hohlraums,” *Phys. Plasmas* **14**, 056312 (2007).
- <sup>26</sup>H. Robey, P. Amendt, J. Milovich *et al.*, “Hohlraum-driven mid-Z (SiO<sub>2</sub>) double-shell implosions on the omega laser facility and their scaling to NIF,” *Phys. Rev. Lett.* **103**, 145003 (2009).
- <sup>27</sup>J. W. Li, W. B. Pei, X. T. He *et al.*, “Preheat of radiative shock in double-shell ignition targets,” *Phys. Plasmas* **20**, 082707 (2013).
- <sup>28</sup>B. Scheiner, M. J. Schmitt, S. C. Hsu *et al.*, “First experiments on Revolver shell collisions at the OMEGA laser,” *Phys. Plasmas* **26**, 072707 (2019).
- <sup>29</sup>E. C. Merritt, J. P. Sauppe, E. N. Loomis *et al.*, “Experimental study of energy transfer in double shell implosions,” *Phys. Plasmas* **26**, 052702 (2019).
- <sup>30</sup>M. A. Barrios, S. P. Regan, K. B. Fournier *et al.*, “X-ray area backlighter development at the National Ignition Facility (invited),” *Rev. Sci. Instrum.* **85**, 11D502 (2014).
- <sup>31</sup>K. Molvig, M. J. Schmitt, B. J. Albright *et al.*, “Low fuel convergence path to direct-drive fusion ignition,” *Phys. Rev. Lett.* **116**, 255003 (2016).
- <sup>32</sup>J. A. King, K. Akli, B. Zhang *et al.*, “Ti K $\alpha$  radiography of Cu-doped plastic microshell implosions via spherically bent crystal imaging,” *Appl. Phys. Lett.* **86**, 191501 (2005).
- <sup>33</sup>H. Sawada, S. Lee, T. Shiroto *et al.*, “Flash K $\alpha$  radiography of laser-driven solid sphere compression for fast ignition,” *Appl. Phys. Lett.* **108**, 254101 (2016).
- <sup>34</sup>H. S. Park, B. R. Maddox, E. Giraldez *et al.*, “High-resolution 17–75 keV backlighters for high energy density experiments,” *Phys. Plasmas* **15**, 072705 (2008).
- <sup>35</sup>R. Tommasini, A. MacPhee, D. Hey *et al.*, “Development of backlighting sources for a Compton radiography diagnostic of inertial confinement fusion targets (invited),” *Rev. Sci. Instrum.* **79**, 10E901 (2008).
- <sup>36</sup>E. Brambrink, H. G. Wei, B. Barbrel *et al.*, “Direct density measurement of shock-compressed iron using hard x rays generated by a short laser pulse,” *Phys. Rev. E* **80**, 056407 (2009).
- <sup>37</sup>R. Tommasini, S. P. Hatchett, D. S. Hey *et al.*, “Development of Compton radiography of inertial confinement fusion implosions,” *Phys. Plasmas* **18**, 056309 (2011).
- <sup>38</sup>B. Borm, D. Khaghani, and P. Neumayer, “Properties of laser-driven hard x-ray sources over a wide range of laser intensities,” *Phys. Plasmas* **26**, 023109 (2019).
- <sup>39</sup>R. Tommasini, O. L. Landen, L. Berzak Hopkins *et al.*, “Time-resolved fuel density profiles of the stagnation phase of indirect-drive inertial confinement implosions,” *Phys. Rev. Lett.* **125**, 155003 (2020).
- <sup>40</sup>C. Tian, M. H. Yu, L. Q. Shan *et al.*, “Radiography of direct drive double shell targets with hard x-rays generated by a short pulse laser,” *Nucl. Fusion* **59**, 046012 (2019).
- <sup>41</sup>K. Du, M. F. Liu, T. Wang, X. S. He, Z. W. Wang, and J. Zhang, “Recent progress in ICF target fabrication at RCLF,” *Matter Radiat. Extremes* **3**, 135 (2018).
- <sup>42</sup>Z. C. Li, X. H. Jiang, S. Y. Liu *et al.*, “A novel flat-response x-ray detector in the photon energy range of 0.1–4 keV,” *Rev. Sci. Instrum.* **81**, 073504 (2010).
- <sup>43</sup>F. Zhang, J. Li, L. Q. Shan *et al.*, “Measurement of the injecting time of picosecond laser in indirect-drive integrated fast ignition experiments using an x-ray streak camera,” *Rev. Sci. Instrum.* **90**, 033504 (2019).
- <sup>44</sup>C. D. Chen, J. A. King, M. H. Key *et al.*, “A Bremsstrahlung spectrometer using k-edge and differential filters with image plate dosimeters,” *Rev. Sci. Instrum.* **79**, 10E305 (2008).
- <sup>45</sup>R. Ramis, R. Schmalz, and J. Meyer-ter-Vehn, “MULTI—A computer code for one-dimensional multigroup radiation hydrodynamics,” *Comput. Phys. Commun.* **49**, 475 (1988).
- <sup>46</sup>R. Ramis, B. Canaud, M. Temporal, W. J. Garbett, and F. Philippe, “Analysis of three-dimensional effects in laser driven thin-shell capsule implosions,” *Matter Radiat. Extremes* **4**, 055402 (2019).
- <sup>47</sup>S. Agostinelli, J. Allison, K. Amako *et al.*, “Geant4—A simulation toolkit,” *Nucl. Instrum. Methods Phys. Res., Sect. A* **506**, 250 (2003).
- <sup>48</sup>J. Allison, K. Amako, J. E. A. Apostolakis *et al.*, “Geant4 developments and applications,” *IEEE Trans. Nucl. Sci.* **53**, 270 (2006).
- <sup>49</sup>J. Allison, K. Amako, J. Apostolakis *et al.*, “Recent developments in Geant4,” *Nucl. Instrum. Methods Phys. Res., Sect. A* **835**, 186 (2016).
- <sup>50</sup>S. Chen, G. Golovin, C. Miller *et al.*, “Shielded radiography with a laser-driven MeV-energy X-ray source,” *Nucl. Instrum. Methods Phys. Res., Sect. B* **366**, 217 (2016).
- <sup>51</sup>K. Lan, J. Liu, Z. C. Li *et al.*, “Progress in octahedral spherical hohlraum study,” *Matter Radiat. Extremes* **1**, 8 (2016).
- <sup>52</sup>Y. Ping, V. A. Smalyuk, P. Amendt *et al.*, “Enhanced energy coupling for indirectly driven inertial confinement fusion,” *Nat. Phys.* **15**, 138 (2019).
- <sup>53</sup>L. Jing, S. Jiang, L. Kuang *et al.*, “Preliminary study on a tetrahedral hohlraum with four half-cylindrical cavities for indirectly driven inertial confinement fusion,” *Nucl. Fusion* **57**, 046020 (2017).
- <sup>54</sup>L. Antonelli, S. Atzeni, A. Schiavi *et al.*, “Laser-driven shock waves studied by x-ray radiography,” *Phys. Rev. E* **95**, 063205 (2017).
- <sup>55</sup>R. Tommasini, C. Bailey, D. K. Bradley *et al.*, “Short pulse, high resolution, backlighters for point projection high-energy radiography at the National Ignition Facility,” *Phys. Plasmas* **24**, 053104 (2017).